Chinese Chemical Letters 35 (2024) 108591

Contents lists available at ScienceDirect

Chinese Chemical Letters

journal homepage: www.elsevier.com/locate/cclet

Plasmon Bi *in-situ* anchored on BiOCl nanosheets assembled microspheres towards optimized photothermal-photocatalytic performance

Dongxue Song[a], Mingxia Li[a,*], Fan Yang[a], Menghan Yu[a], Zhenzi Li[b], Jie Chen[a], Xiaoshuang Zhang[a], Wei Zhou[a,b,*]

[a] *School of Chemistry and Materials Science, Key Laboratory of Functional Inorganic Material Chemistry, Ministry of Education of the People's Republic of China, Heilongjiang University, Harbin 150080, China*
[b] *Shandong Provincial Key Laboratory of Molecular Engineering, School of Chemistry and Chemical Engineering, Qilu University of Technology (Shandong Academy of Sciences), Ji'nan 250353, China*

ARTICLE INFO

Article history:
Received 27 September 2022
Revised 17 May 2023
Accepted 18 May 2023
Available online 19 May 2023

Keywords:
Photocatalysis
BiOCl
Heterojunction
Plasmon Bi
Mesoporous structure

ABSTRACT

Interface engineering is of great importance to improve the photocatalytic performance. Herein, *in-situ* formation plasmon Bi/BiOCl nanosheets assembled heterojunction microspheres are fabricated *via* facile reductive solvothermal approach. The aldehyde group in the DMF structure is used to exert the weak reducing property of the solvent and thus strip out the metal Bi in BiOCl. The metal Bi is anchored on surface of BiOCl firmly due to *in-situ* formation engineered interface, which could realize efficient charge transfer channel. The resultant Bi/BiOCl heterojunctions assemblies with narrow bandgap of 3.05 eV and mesoporous structure extend the photoresponse to visible light region and could provide sufficient surface active sites. The visible-light-driven photocatalytic degradation of high-toxic norfloxacin for Bi/BiOCl heterojunctions is up to 95.5% within 20 min, representing several times that of pristine BiOCl nanosheets and the physical mixture. It is attributed to the *in-situ* formation of Bi/BiOCl heterojunctions and surface plasmon resonance (SPR) effect of plasmon Bi promoting charge transfer, and the obvious photothermal effect promoting the photocatalytic reaction, which are verified by experimental and density functional theory (DFT) calculations. This strategy provides ideal perspectives for fabricating metal/semiconductor heterojunctions photocatalysts with high-performance.

As a two-dimensional material, BiOCl has frequently received widespread attention as a promising photocatalyst because of its special interlayer structure consisting of a combination of bis-Cl^- and $[Bi_2O_2]^{2+}$ [1–3]. This structure enhances the utilization of BiOCl for light quantum efficiency, as well as the interlayer structure connected by van der Waals forces, which will also reduce excitonic complexation [4,5]. Moreover, due to the inhomogeneous charge distribution between $[Bi_2O_2]^{2+}$ and Cl^- layers, built-in electric fields can be formed spontaneously to drive the separation and transfer of photogenerated charge carriers. BiOCl with its different geometries and electronic structures can be well advanced in the field of photocatalysis [6]. However, single-phase BiOCl with a large bandgap of about 3.37 eV has a higher photogenerated electron-hole complexation rate [7], which can only absorb ultraviolet light. Nevertheless, UV light accounts for a very limited proportion (~5%) of the solar energy, so the photocatalytic efficiency in natural environment is not satisfactory. Therefore, some BiOCl modifications have been made to create oxygen vacancy defects to improve the photocatalytic oxidation capacity [8,9]. Furthermore, Wang *et al.* [10] created BiOCl nanosheets with Bi vacancies and exposed (001) crystalline surfaces of self-assembled rose-shaped two-dimensional materials with adequate active sites for efficient CO_2 capture and reduction. Alternatively, heterojunctions are ideal candidates to be constructed by compounding with other semiconductors [11,12]. Such methods could promote spatial charge separation and improve photocatalytic activity obviously.

Among them, the most prevalent is the assembly of noble metals and semiconductors (such as Au, Ag, and Pt) [13,14]. Li *et al.* [15] reported metal Au loaded on BiOCl nanospheres containing oxygen vacancies to oxidize benzyl alcohol to benzaldehyde with more than 99% selectivity under commercially available light using the synergistic effect of plasma hot electrons and holes. This study

* Corresponding authors.
E-mail addresses: limingxia@hlju.edu.cn (M. Li), zwchem@hotmail.com (W. Zhou).

https://doi.org/10.1016/j.cclet.2023.108591
1001-8417/

dramatically improved the photocatalytic performance of BiOCl. However, this stepwise synthesis of metal-semiconductor composite suffers from the drawback of poor interfacial coupling. And the post-loading process tends to make the photogenerated charge carriers recombined at the interface, which makes high charge separation resistance. As a result, constructing an effective interfacial coupling for improving the transfer efficiency of photogenerated charge carriers is an ideal issue to be considered. Then compared to precious metals, it has been found that metal Bi, a cheap, harmless and well-conducting metal, can also possess surface plasmon resonance (SPR) effects. Metal Bi not only enhances the ability to capture light but also promotes the separation of charge carriers, resulting in enhanced photocatalytic activity [16–19]. In summary, the common problems are interface engineering between Bi and BiOCl, which result in low charge separation efficiency. Therefore, how to design intimate coupling interface between Bi and BiOCl is still a great challenge to further improve the spatial charge separation.

In this work, *in-situ* formation Bi/BiOCl heterojunction assembly microspheres were fabricated by a simple solvothermal strategy. The *in-situ* generation of metal Bi in the reduction system was used to achieve tight interface coupling between Bi and BiOCl, which solved the charge separation resistance problem. The *in-situ* grown Bi/BiOCl has the advantages of surface mesoporous structure, high specific surface area and anti-stacking, *etc.* The generated Bi has the characteristics of high dispersion and strong contact making obvious SPR effect and photothermal effect. In this way, the photocatalyst formed by metal Bi and BiOCl had a close contact heterogeneous interface, rapid photogenerated carrier transfer, and high charge separation efficiency. The resultant Bi/BiOCl heterojunction photocatalysts exhibited superior photocatalytic activity towards the degradation of norfloxacin. And the excellent electron transfer capability of metal Bi to BiOCl was further demonstrated by density functional theory (DFT) calculations. A mechanism of possible photocatalysis is also proposed.

Bismuth nitrate pentahydrate ($Bi(NO_3)_3{\cdot}5H_2O$) was purchased from Shanghai Dibai Biotechnology Co., Ltd., Potassium chloride (KCl) was purchased from Tianjin Guangfu Technology Development Co., Ltd., and *N*,*N*-dimethylformamide (DMF) was purchased from Tianjin Fuyu Fine Chemical Co., Ltd. All the above chemicals are analytical grade and used without further purification.

Catalyst was prepared by the classical solvothermal method. 2.9 g $Bi(NO_3)_3{\cdot}5H_2O$ and 0.44 g KCl were added to 32 mL DMF solvent, then stirred the solution at high speed for 30 min, and the solution was added to a 50 mL polytetrafluoroethylene (PTFE) lined stainless steel autoclave for continuous reaction at 160 °C for 6, 12, 18, 24 h, respectively. After the reaction, the mixture was washed three times with water and ethanol, respectively. The sample was dried at 70 °C for 12 h. The collected sample was denoted as Bi/BiOCl.

2.9 g $Bi(NO_3)_3{\cdot}5H_2O$ and 0.44 g KCl were added to 32 mL distilled water, then stirred the solution for 30 min, and added the solution to a 50 mL PTFE lined stainless steel autoclave for continuous reaction at 160 °C for 12 h. After the reaction, the mixture was washed three times with water and ethanol, respectively. The sample was dried at 70 °C for 12 h and finally collected, which was denoted as BiOCl.

Scheme 1 shows a schematic diagram for the formation of Bi/BiOCl microspheres. Relying on the relative weak reducibility of DMF, BiOCl nanosheets without metal Bi are formed at 120 °C by a simple solvothermal method, and metal Bi is formed *in-situ* on BiOCl at 160 °C to form self-assembled Bi/BiOCl microspheres.

Fig. 1a is a scanning electron microscopy (SEM) image and shows that BiOCl is structured as a two-dimensional nanosheet, and the width of the nanosheet is 1–2 μm, but the formed nanosheets gather together due to electrostatic action and van der

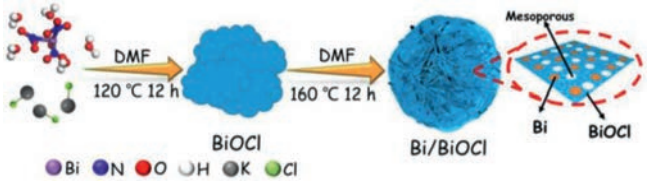

Scheme 1. Schematic illustration for the formation of Bi/BiOCl nanosheets assembled microspheres.

Waals force. Fig. 1b shows the structure of Bi/BiOCl composites assembled from nanosheets into microspheres of about 20 μm in size, which is due to the large surface free energy and specific surface area on the surface of the nanosheets, resulting in self-assembly to form super large flower-like microspheres [4,20]. The SEM image of Fig. 1c clearly shows a microsphere composed of numerous ultrathin nanosheets self-assembled against stacking. Figs. S1a and b (Supporting information) are SEM images of samples at 120 and 140 °C, respectively, where Fig. S1a demonstrates a slight aggregation of the nanosheets of BiOCl, and Fig. S1b is a microsphere formed by the aggregation of Bi/BiOCl, but the binding is not as tight as that of Bi/BiOCl at 160 °C. Fig. 1d shows the SEM image of Bi/BiOCl and Figs. 1e-g show the corresponding element mapping distribution among Bi, O, and Cl respectively, which can prove that Bi, O, and Cl are uniformly dispersed in Bi/BiOCl. Additionally, the energy dispersive X-ray (EDX) in Fig. 1h can also prove that Bi, O, and Cl elements coexist in the sample and no other redundant peaks appear. Figs. 1i-k are transmission electron microscopy (TEM) and high-resolution TEM (HRTEM) images to further characterize Bi/BiOCl. Figs. 1i and j show that Bi/BiOCl is an ultrathin nanosheet structure, and there are many metal Bi nanoparticles on surface of BiOCl nanosheets. Furthermore, as shown in Fig. 1k, the HRTEM image can be found in the presence of two kinds of lattices, in which the 0.322 nm lattice stripe belongs to the (012) crystal plane of metal Bi nanoparticles, and the 0.276 nm lattice stripe belongs to the (110) crystal plane of BiOCl nanosheets. This confirms the formation of metal Bi and BiOCl. From the above results, it can be confirmed that there is intimate contact between Bi and BiOCl firmly because of the Bi *in-situ* anchored on BiOCl.

Fig. 2a shows the X-ray diffraction (XRD) patterns of BiOCl and Bi/BiOCl. In single-phase BiOCl, the crystallinity is high and there are no impurity peaks. There are eight typical peaks of BiOCl in Bi/BiOCl, which are at $2\theta = 12.0°$, 25.9°, 32.6°, 33.6°, 46.8°, 54.2°, 58.8° and 68.3°, the corresponding crystal planes are (001), (011), (110), (102), (020), (121), (122) and (220), respectively, indexed as BiOCl (JCPDS No. 73–2060). In Bi/BiOCl, there are obvious peaks of metal Bi at $2\theta = 27.2°$, 37.9°, 39.6°, 44.5°, 48.7°, 56.0°, 62.2°, 64.5°, the indexable corresponding crystal planes are (012), (104), (110), (015), (202), (024), (116) and (122), (JCPDS no. 85–1329). The XRD peaks of Bi/BiOCl are broadened compared to those of BiOCl. The reason is that with the precipitation of metal Bi, the particle size of metal Bi increases, some defects forms and the overall structure symmetry decreases in the reaction process, leading to the broadening of the XRD peak. The two BiOCl crystals belong to the same space group P4/nmm (No. 129) [21]. Table S1 (Supporting information) shows the cell parameters of these two catalysts. The cell parameters of BiOCl are $a = b = 3.878$ Å, $c = 7.403$ Å. The unit cell parameters of BiOCl in Bi/BiOCl are $a = b = 3.880$ Å, $c = 7.347$ Å. The changed cell parameters indicate the change of BiOCl microstructure, which is also evidence for the formation of Bi/BiOCl from another point of view. The XRD patterns (Fig. 2b) of Bi/BiOCl regulated at different times shows that the intensity of the diffraction peak of elemental bismuth increases with the reaction time at 6, 12, 18, and 24 h, indicating a higher yield of metallic Bi on BiOCl [22]. From the above analysis, it can be elucidated that the

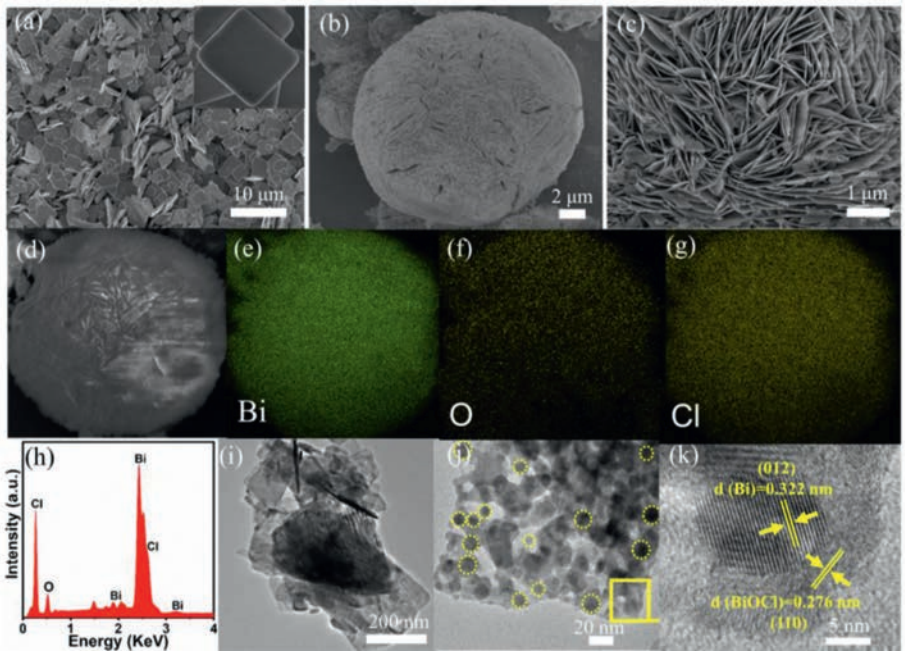

Fig. 1. SEM image of BiOCl (a), SEM images of Bi/BiOCl (b-d). Elemental mappings of Bi (e), O (f), Cl (g). EDX (h), TEM (i, j), and HRTEM images (k) of Bi/BiOCl microspheres.

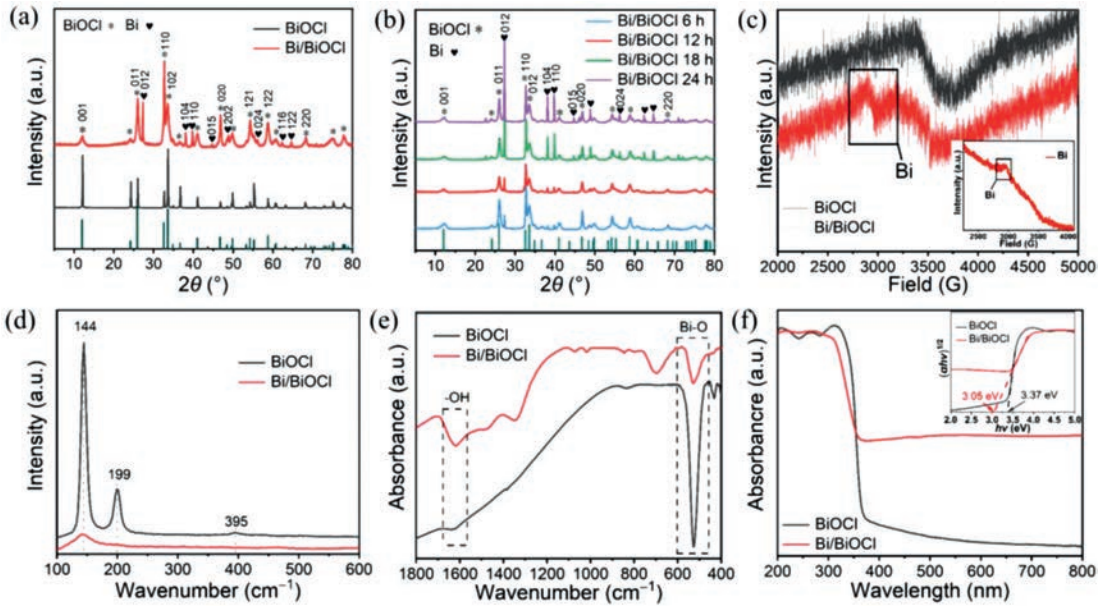

Fig. 2. XRD patterns of BiOCl and Bi/BiOCl (a). XRD patterns of Bi/BiOCl (6 h, 12 h, 18 h, and 24 h) (b). EPR spectra (c) (the inset is the EPR of metal Bi), Raman spectra (d), FT-IR (e), and UV–vis diffuse reflectance spectra (f) (the inset is the bandgap) of BiOCl and Bi/BiOCl, respectively.

content of metal Bi produced in 12 h reaction time is optimized, which will be reflected in the water pollutant degradation. Besides, the formation of Bi/BiOCl at different temperatures were also studied. In Fig. S2 (Supporting information), it is noted that there is no diffraction peak of metal Bi in BiOCl at 120 °C, suggesting that there is no metal Bi formation, while only a little metal Bi appears at 140 °C, which can be observed in the diffraction peak of metal Bi. The presence of metal Bi in the microstructure can be further demonstrated using the electron paramagnetic resonance (EPR) test. In Fig. 2c, it can be found that Bi/BiOCl has a vibration peak of metal Bi at $g = 1.84$, but not in BiOCl. The above two characterization methods can both indirectly prove the existence of metal Bi in Bi/BiOCl. The metal Bi is generated *in-situ* on BiOCl because of the weak reducibility of DMF, which reduces part of Bi^{3+} to metal Bi [23]. The reducibility of DMF is attributed to the presence of aldehyde groups, which play a role in reducing metal cations to metal simple substances, which are oxidized to carboxyl groups as the following equation (Eq. 1):

$$n\mathrm{HCONMe_2} + \mathrm{M}^{n+} + \mathrm{H_2O} \rightarrow \mathrm{M} + n\mathrm{Me_2NCOOH} + 2\mathrm{H}^{+} \quad (1)$$

In order to determine the structure and vibrational peak variations of BiOCl and Bi/BiOCl, Raman spectra were analyzed (Fig. 2d). BiOCl has obvious strong vibration bands at 144 and 199 cm^{-1}, while there is a weak vibration band at 395 cm^{-1}. The vibrational bands 144 and 199 cm^{-1} correspond to the interlayer vibrational mode of A_{1g} and the in-plane Bi-Cl bond stretching of E_g. Similarly, the vibrational band 395 cm^{-1} corresponds to the O-atom antisymmetric stretching of B_{1g}. While the vibration peak of Bi/BiOCl

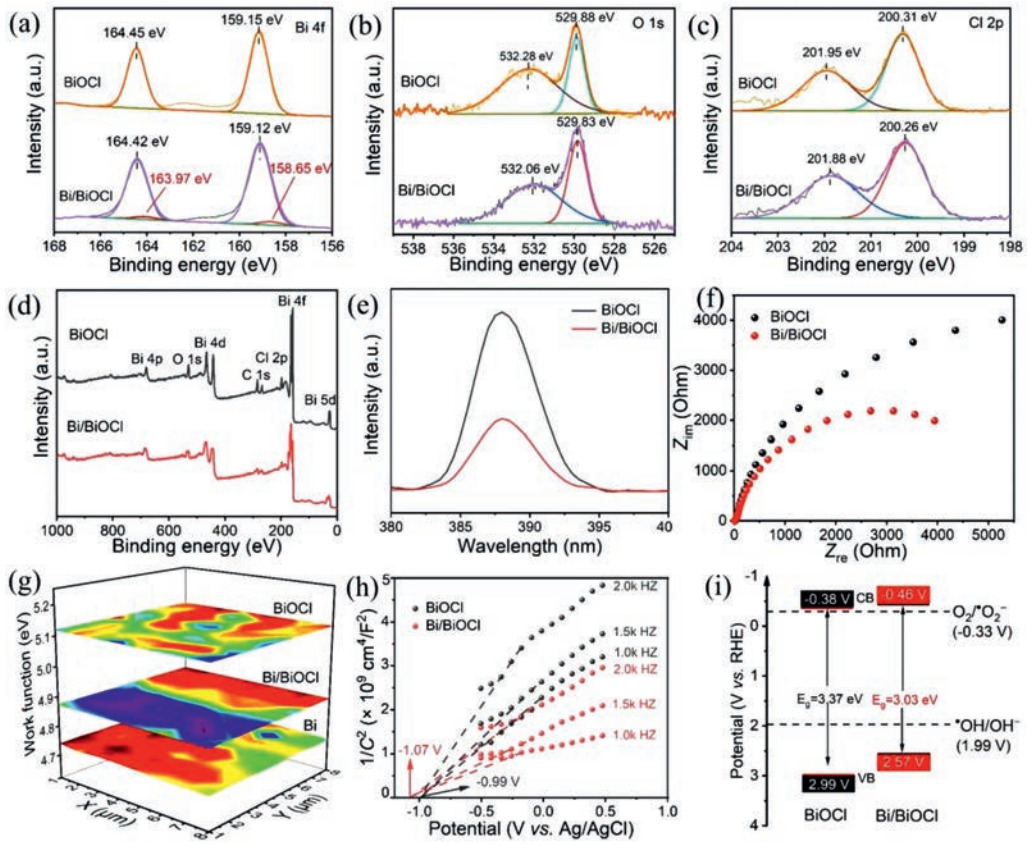

Fig. 3. XPS spectra of Bi 4f (a), O 1s (b), Cl 2p (c). Full-scale XPS spectra (d), steady-state fluorescence spectra (e), and EIS (f) of BiOCl and Bi/BiOCl. SKP maps (g) of Bi, BiOCl, and Bi/BiOCl, respectively. Mott–Schottky plots (h), and band energy diagram *vs.* reversible hydrogen electrode (i) of BiOCl and Bi/BiOCl, respectively.

at 144 cm^{-1} weakens or even disappears at 199 and 395 cm^{-1}, which is due to the weak reduction of DMF leading to partial BiOCl to metal Bi, making the intra-bond stretching weaker [10,24]. The chemical structures of BiOCl and Bi/BiOCl were investigated using Fourier transform infrared spectroscopy (FTIR) (Fig. 2e). The FTIR spectra of BiOCl and Bi/BiOCl show stretching vibration peaks at 526 and 1621 cm^{-1}, which belong to tensile vibration of Bi-O and tensile vibration and bending vibration of -OH group caused by hydration on the sample surface [25]. Fig. 2f shows the UV visible diffuse (UV–vis) to study the optical properties of the sample. It shows that the presence of bismuth causes Bi/BiOCl to possess a stronger continuum absorption band between 400 and 800 nm. For Bi/BiOCl, the absorption intensity in UV region is stronger than BiOCl, suggesting with the presence of metal Bi effectively enhances the light absorption due to the near-UV and visible light absorption of non-noble metal Bi. It shows surface plasmon resonance (SPR) characteristics in visible light range and promotes the utilization of photon energy in the range of ultraviolet and visible light regions [26]. The inset is a bandgap diagram, and the bandgap value (E_g) of the sample can be obtained from Eq. 2:

$$E_g(\text{eV}) = 1240/\lambda \quad (2)$$

where λ refers to the maximum absorption wavelength. The bandgap of BiOCl is estimated to be ~3.37 eV, demonstrating that it cannot absorb visible light [27]. The bandgap of Bi/BiOCl is reduced to ~3.05 eV, and it proves that the existence of metal Bi reduces the bandgap of Bi/BiOCl, which is suitable for visible-light-driven photocatalysis [28]. The results of Brunauer-Emmett-Teller (BET) (Fig. S3 in Supporting information) demonstrate type IV isotherms with H-type hysteresis regression line under higher relative pressures, suggesting a homogeneous distribution of mesopores in BiOCl and Bi/BiOCl [29]. Fig. S4 (Supporting information) shows the pore size distribution curve of Bi/BiOCl, and a wide peak of 20–80 nm can be observed, showing that Bi/BiOCl has mesopores [29]. The specific surface area of Bi/BiOCl (18.4 m^2/g) is around 18 times higher than that of BiOCl (1.0 m^2/g) (Table S2 in Supporting information). And pore size (18.9 nm) and pore volume (0.07 cm^3/g) of Bi/BiOCl are higher than those of BiOCl (16.6 nm and 0.002 cm^3/g). A comparatively high specific surface area and mesoporous structure of Bi/BiOCl can supply sufficient surface active sites for the follow-up photocatalytic reaction.

Figs. 3a-c show X-ray photoelectron spectroscopy (XPS), exhibiting chemical states on BiOCl and Bi/BiOCl surfaces. In XPS spectra, the Bi, O, and Cl elements have been detected from both samples. In Fig. 3a, the binding energies at 159.12 and 164.42 eV corresponding to Bi $4f_{7/2}$ and Bi $4f_{5/2}$ orbits, separately, and they are characteristic peaks of Bi^{3+} [30,31]. Meanwhile, the corresponding Bi^0 characteristic peaks at the binding energies of 158.65 and 163.97 eV for Bi/BiOCl samples demonstrate the presence of metal Bi on the Bi/BiOCl surface [32]. This is consistent with the previous TEM, XRD, and EPR results. As shown in Fig. 3b, there are binding energies at 532.28 and 529.88 eV which belong to the characteristic peaks of hydroxyl oxygen and lattice oxygen, respectively [33]. Fig. 3c illustrates that the binding energies at 200.31 and 201.95 eV belong to Cl $2p_{3/2}$ and Cl $2p_{1/2}$ characteristic peaks, respectively. Meanwhile, in the full-scale XPS spectra of Fig. 3d, it can be further confirmed that the Bi/BiOCl sample contains only Bi, O, and Cl, and there are no other interference elements. Moreover, in the valence band spectra (Fig. S5 in Supporting inforamtion), it can be seen that the valence band (2.02 eV) of Bi/BiOCl is smaller than that of BiOCl (2.21 eV), which proves that metal Bi increases the maximum valence band value of Bi/BiOCl and reduces

the bandgap. As shown in Fig. 3e, the separation efficiency of the electron-hole pairs is analyzed by steady-state photoluminescence spectroscopy (PL). The peak intensity of Bi/BiOCl at the emission peak around 388 nm is much weaker than BiOCl, indicating that Bi/BiOCl reduces the recombination of photo-generated electron-hole pairs, thus having a longer excitation lifetime and higher separation efficiency. It also proves that photogenerated electrons in the energy band structure may flow from the metal Bi to BiOCl [34]. Additionally, the transient luminescence spectra (Fig. S6 in Supporting information) tests expressed that the excitation life of Bi/BiOCl is longer than that of BiOCl, which confirm that the appropriate metal Bi content in Bi/BiOCl plays a vital role on the effective separation of photogenerated charge carriers for photocatalysis [29,35]. The electrochemical impedance spectroscopy (EIS) is applied to explore the efficiency of charge separation in photocatalysts (Fig. 3f). Compared with the two samples under light conditions, Bi/BiOCl has less curvature, suggesting that the resistance is lower and the transfer and separation efficiency is higher. The appearance of metal Bi enhances the charge separation process, which affects the distribution of electric double layers and promotes electron transport, making the electric transfer resistance significantly decreased to facilitate the separation of electron-hole pairs [36]. This is consistent with the PL results. Fig. 3g is a scanning Kelvin probe microscope (SKP), a surface potential measurement technique that measures the work functions or surface potentials of materials. The work function (W_F) can be calculated according to Eq. 3:

$$W_F(\text{eV}) = 5.1 + \frac{\Delta\text{CPD}}{1000} \tag{3}$$

where ΔCPD is the contact potential difference. The work functions of metal Bi, BiOCl, and Bi/BiOCl are calculated to be *ca.* 4.73, 5.18, and 4.88 eV, respectively. The metal Bi has a lower Fermi level than BiOCl, demonstrating that the electron flow direction is from metal Bi to BiOCl. The Bi/BiOCl has a lower Fermi level than BiOCl, with this changing the surface band bending and forming built-in electric field [4]. The heterostructure of Bi/BiOCl accelerates the charge transfer from the interface, which decreases the recombination of electrons and holes, thereby improving the photocatalytic performance. Fig. 3h shows Mott-Schottky diagrams of BiOCl and Bi/BiOCl at three frequencies (1.0, 1.5, and 2.0 kHz), which can determine the flat band potentials. It can be noted that the slopes of BiOCl and Bi/BiOCl are positive, indicating that materials are n-type semiconductors. As shown in Fig. 3h, the flat-band potentials are the *x*-axis intercept of BiOCl and Bi/BiOCl, which are −0.99 and −1.07 V individually, indicating the increase of Fermi level for Bi/BiOCl. The results are consistent with SKP measurements. The carrier concentration (N_d) can be calculated from Eq. 4:

$$N_d = \left(\frac{2}{e_0 \varepsilon \varepsilon_0}\right)\left(\frac{d\frac{1}{C^2}}{dV}\right)^{-1} \tag{4}$$

where e_0 is the charge per-unit charge, ε is the relative permittivity, ε_0 is the vacuum permittivity, C is the interfacial capacitance, and V is the voltage. It takes $\varepsilon_0 = 55$ for BiOCl [37]. The carrier concentrations of BiOCl and Bi/BiOCl are $N_d = 1.22 \times 10^{19}$ and $N_d = 2.66 \times 10^{19}$, respectively. The carrier concentration in semiconductor materials directly determines the conductivity of semiconductors, which can prove that Bi/BiOCl has stronger conductivity and better photocatalytic activity than that of BiOCl. Since the conduction band (CB) bottom of the n-type semiconductor is nearly flat-band potential as the calculation formula (Eq. 5):

$$E(\text{RHE}) = E(\text{Ag/AgCl}) + 0.0591\text{pH} + 0.197 \tag{5}$$

where E is the electrode potential. The values for the CB positions of BiOCl and Bi/BiOCl are calculated to be −0.38 and −0.46 V, respectively. According to bandgap width, the complete reversible hydrogen electrode (RHE) can be obtained [2,38]. In Fig. 3i, it can be observed that the CB position of BiOCl is lower than that of Bi/BiOCl, showing that the electron direction in the metal Bi is transferred from Bi to BiOCl. Considering the wide light absorption of metal Bi, it showed an obvious photothermal effect (Fig. S7 in Supporting information). Both have an onset temperature of 30 °C. Fig. S7a presents the photothermal effect of BiOCl with a central temperature increases from 30.0 °C to 49.5 °C (6 min). Fig. S7b shows the center temperature increases from 30.2 °C to 55.0 °C (6 min), which proves the existence of the good photothermal effect for Bi/BiOCl. Compared with BiOCl, Bi/BiOCl has more obvious photothermal effect, owing to the surface plasmon resonance (SPR) effect of Bi combined with BiOCl strengthening the absorption ability of sunlight [39].

In order to further reveal the electronic properties of BiOCl and Bi/BiOCl assembly, DFT calculations with analysis of the density of states (DOS) and work functions were performed to investigate the possible electron transfer between Bi and BiOCl using the VASP package. The details of the VASP calculation are available in the supporting information. The charge density difference is shown in Fig. 4a, in which blue and yellow colors stand for losing and gaining electrons, respectively. It is clear that the electron of metal Bi is transferred to the surface of BiOCl, which endows BiOCl with a large number of electrons to form a built-in electric field, becoming a photocatalytic active center [22]. Figs. 4b-d are the diagram of DOS of Bi, BiOCl, and Bi/BiOCl, respectively, in which the total DOS of composite and the partial DOS of element Bi, O, and Cl are all provided. As seen in Figs. 4c and d, the TDOS of BiOCl is a semiconductor with an obvious bandgap, but after combination with Bi, the 6p state of metal Bi appears above the Fermi level, indicating the composite has strong conductivity. In the region of the valence band near the Fermi level, there is an overlap between the 2p state of O and the 6p state of metal Bi, suggesting a strong electron interaction between Bi and BiOCl. The obvious 6p state of metal Bi and Bi in BiOCl appear in the conduction band region near the Fermi level, demonstrating their strong ability to accept electrons of them. Both the two couplings promote electron transfer and the generation of photogenerated charge carriers [40]. Figs. 4e-g show the work function diagrams of Bi, BiOCl, and Bi/BiOCl. The influence of composite materials on electron distribution can be reflected by the work function, which can be determined theoretically and experimentally. From the work function diagrams, it can be noticed that the emergence of metal Bi reduces the work function of BiOCl to promote the transfer of electrons from Bi to BiOCl, which is consistent with the results of the above differential charge distribution and previous experimental observation as shown in Fig. 3g.

In recent years, norfloxacin has been detected in different water resources, and even in drinking water at levels of ng/L∼μg/L in them. [41]. Considering the universality and risk of norfloxacin pollution, it urgently needs an efficient and practical method to remove norfloxacin from the aqueous environment. Thus, the *in-situ* grown Bi/BiOCl material is applied to photocatalytic degradation of norfloxacin. As shown in Fig. 5a, the time-varying absorption spectra of norfloxacin by Bi/BiOCl. It can be expected that the spectral intensity hardly changes with the increase of time during dark treatment under the highest absorption wavelength of 264 nm, suggesting that the self-degradation is not significant. The spectral intensity decreased sharply after illumination, indicating that Bi/BiOCl has a pretty decent degradation ability of norfloxacin under visible light irradiation [42]. The content of metal Bi in Bi/BiOCl was further determined by the thermogravimetric analysis test (TG). A sharp decrease in weight at 650–800 °C can be found in the TG curve (Fig. S8 in Supporting information), and finally a platform appears after 800 °C. After combustion, the weight of the remaining single-phase BiOCl is 78.8 wt%, and the weight

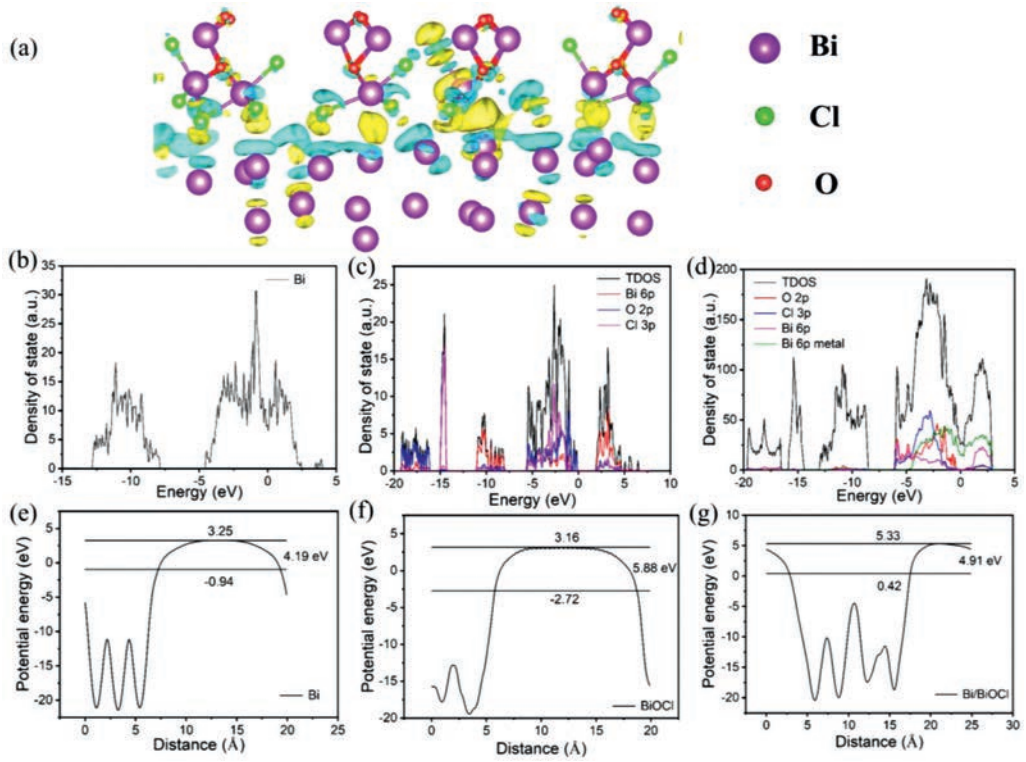

Fig. 4. (a) Charge density differences of Bi/BiOCl. DOS of Bi (b), BiOCl (c), and Bi/BiOCl (d). Work functions of Bi (e), BiOCl (f), and Bi/BiOCl (g), respectively.

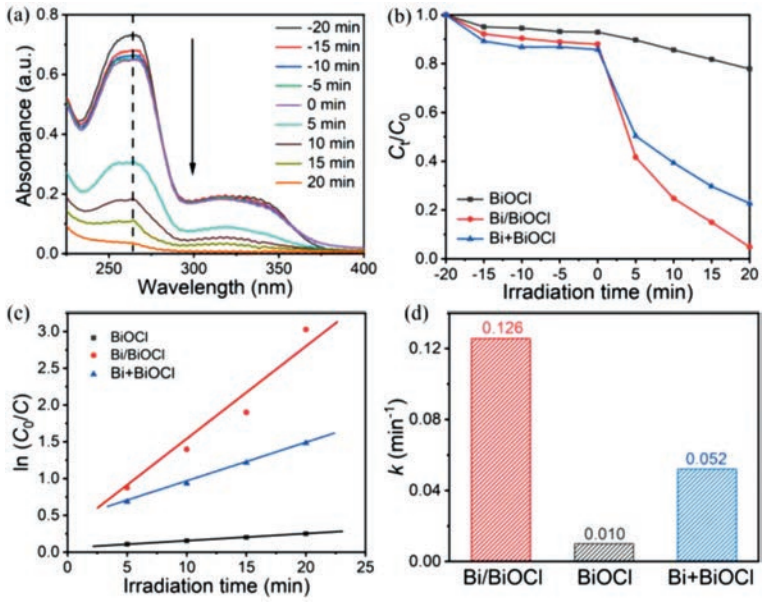

Fig. 5. (a) Time varying absorption spectra of Bi/BiOCl for photocatalytic degradation norfloxacin. (b) Photocatalytic degradation curves of norfloxacin. Rate curves (c) and rate constants (d) of BiOCl, Bi/BiOCl, and Bi+BiOCl, respectively.

of the remaining Bi/BiOCl is 92.9 wt%. According to the relative mass, it can be calculated that the weight of the metal Bi in the Bi/BiOCl sample is ~7 wt% [43]. To further measure the photocatalytic activity of Bi/BiOCl, the metal Bi is mechanically mixed with BiOCl to synthesize 7% Bi+BiOCl (pure BiOCl without metal Bi could be obtained by reacting in DMF solvent for 1 h, and then BiOCl was ground with 7 wt% of metal Bi in a ball mill for about 6 h). Fig. 5b shows the norfloxacin photocatalytic degradation performance of BiOCl, *in-situ* grown Bi/BiOCl, and mechanically mixed Bi+BiOCl materials. After dark treatment for 20 min, the photocatalytic degradation rate of Bi/BiOCl could be up to 95.2% under visible light irradiation within just 20 min, while the degradation rate of BiOCl could only be 22.1%. As well as the degradation rate of mechanically synthesized Bi+BiOCl is only 77.2%, which was 18% lower than that of Bi/BiOCl. The photocatalytic performance of Bi/BiOCl is better than those of most literatures of BiOCl-based materials (Table S3 in Supporting information). The results indicate the more efficient charge transfer and separation in Bi/BiOCl than that of the physical mixture due to the intimate interface *via in-situ* formation. The degradation rate of Bi/BiOCl is 4.3 and 1.2 times

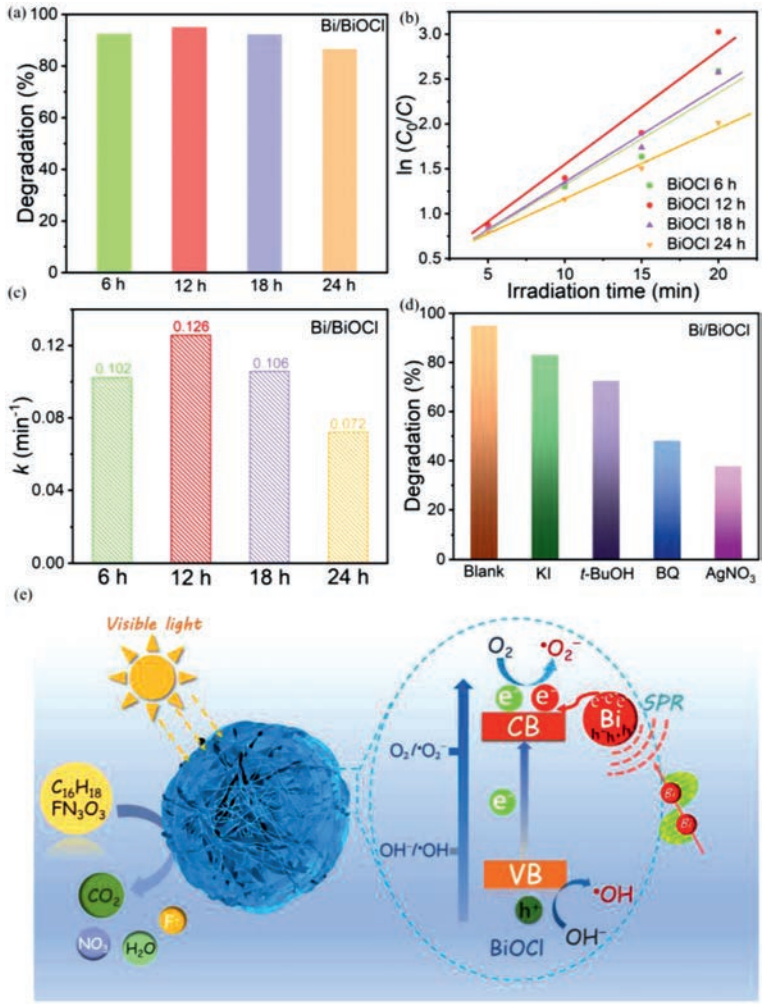

Fig. 6. Histograms of photocatalytic degradation rates (a), rate curves (b), and rate constants (c) of Bi/BiOCl (6 h, 12 h, 18 h, and 24 h). (d) Inhibition of norfloxacin degradation by free radical scavengers in the Bi/BiOCl system. (e) The proposed photocatalytic mechanism of Bi/BiOCl heterojunction assembly under visible light irradiation.

greater than both BiOCl and Bi+BiOCl. Such a significant degradation rate of Bi/BiOCl is due to the synergistic effect of Bi and the interface engineering of BiOCl [18,44]. The reaction kinetics of norfloxacin are fitted according to the first-order kinetic equation, as shown in Eq. 6:

$$\ln(C_0/C) = kt \tag{6}$$

where C_0 is the initial concentration of norfloxacin, C is the actual concentration when the reaction time is t, and k is the reaction kinetic constant. The rate curves of BiOCl, Bi/BiOCl, and Bi + BiOCl are shown in Fig. 5c. It can be visualized that between $\ln(C_0/C)$ and t follow the first-order kinetic curve. Furthermore, as shown in Fig. 5d, the dynamic constants of BiOCl, Bi/BiOCl, and Bi+BiOCl are estimated to be *ca.* 0.01, 0.126, and 0.052, respectively. It is calculated that the dynamic constants of Bi/BiOCl are 12.6 and 2.4 times higher than those of BiOCl and Bi+BiOCl, showing that not only the metal Bi enhances the degradation effect of BiOCl but also the strong interface contact between metal Bi and BiOCl is conducive to charge transfer, which further confirms that Bi/BiOCl has a good prospect in the environmental applications. The close interface coupling of Bi/BiOCl provides a good solution for photocatalytic degradation of pollutant norfloxacin, which indicates that the efficient interface engineering is vital for promoting photogenerated charge transfer and separation, thereby improving the photocatalytic performance.

The influence of reaction time on the photocatalytic degradation performance of Bi/BiOCl was further investigated, and the Bi/BiOCl with different preparation reaction times (6, 12, 18, and 24 h) were degraded norfloxacin by the control variable method (Fig. 6a). The degradation rates of the four samples are 92.5%, 95.2%, 92.4%, and 86.6%, respectively. It can be found that the photocatalytic degradation activity of Bi/BiOCl at 12 h is optimized, which is reflected in the kinetic curve and kinetic constant. In Fig. 6b, it can be identified that the four samples conform to the first-order kinetic curve. The kinetic constants of Bi/BiOCl at 6, 12, 18, and 24 h are estimated to be 0.102, 0.126, 0.106, and 0.072, respectively (Fig. 6c). It can be concluded that Bi/BiOCl with a reaction time of 12 h has the optimized metal Bi content, which provides feasible active sites in photocatalytic reaction [45]. It is well known that the photocatalytic degradation process involves four reactive species, *i.e.*, $^{\bullet}OH$, $^{\bullet}O_2^-$, h^+ and e^-. The primary and secondary reactive species can be determined by a free radical capture experiment. In Fig. 6d, compared with the blank experiment, benzoquinone (BQ), silver nitrate ($AgNO_3$), potassium iodide (KI), and Tert-butanol (*t*-BuOH) are used to capture superoxide anion, electron, holes, and captures hydroxyl groups, respectively [46,47]. After adding BQ and $AgNO_3$, it is found that the photocatalytic degradation rate decreases significantly, demonstrating that the active species are mainly e^- and $^{\bullet}O_2^-$ in this system. As shown in the proposed photocatalytic mechanism diagram (Fig. 6e), Bi/BiOCl is a microsphere composed of nanosheets, which has

a tight coupling structure to accelerate charge transfer and also inhibits the aggregation of nanosheets. At the same time, the SPR effect of metal Bi promoted the separation of electrons and holes of BiOCl, making the degradation of norfloxacin antibiotics into CO_2, H_2O, and other small molecules. And the metal Bi could also show obvious photothermal effect, which could further promote the photocatalytic performance. Under visible light irradiation, electrons transfer from VB to CB of BiOCl, and holes are left in the microsphere structure of Bi/BiOCl to promote the formation of OH^- to $^{\bullet}OH$. In addition, the *in-situ* reduced elemental Bi also transfers its electrons to CB of BiOCl through the SPR effect, and O_2 is converted to $^{\bullet}O_2^-$, which are both reactive species during photocatalytic process as discussed above [22]. The efficient charge transfer and separation between Bi and BiOCl is of great importance to improve the photocatalytic performance. After interface engineering, the *in-situ* formation of Bi could be anchored on surface of BiOCl intimately, which could form efficient bridge for charge transfer and inhibit the recombination. This is important factor for the excellent photocatalytic performance.

In summary, *in-situ* plasmon Bi/BiOCl heterojunction assembly microspheres were formed by a simple solvothermal synthesis method, which formed the closely interface coupling to enhance the charge transfer efficiency. The degradation rate of Bi/BiOCl was 4.3 times greater than that of BiOCl. The photocatalytic rate constants of Bi/BiOCl were estimated to be 12.6 and 2.4 times greater than those of BiOCl and the physical mixture, respectively. This could be ascribed to the formation of *in-situ* plasmon Bi/BiOCl heterojunction and the SPR effect of Bi favoring charge transfer and separation, as well as the obvious photothermal effect promoting the photocatalytic activity. Experimental and DFT calculations both proved the charge transfer directions, which favored improving the final photocatalytic performance obviously. Especially, the *in-situ* formation plasmon Bi anchored on BiOCl facilitated the charge transfer greatly. In addition, the capture experiments confirmed that electrons and $^{\bullet}O_2^-$ were both active species in this photocatalytic system. The high-efficient visible light photocatalysts will have prospective applications in the environmental field.

Declaration of competing interest

The authors declare that they have no known competing financial interests or personal relationships that could have appeared to influence the work reported in this paper.

Acknowledgments

We gratefully acknowledge the support of the National Natural Science Foundation of China (Nos. 52172206 and 21871078), the Heilongjiang Province Natural Science Foundation (No. LH2021B021), and the Development Plan of Youth Innovation Team in Colleges and Universities of Shandong Province.

References

[1] Q. Wang, Z. Miao, Y. Zhang, et al., ACS Catal. 12 (2022) 4016–4025.
[2] Y. Shiraishi, M. Hashimoto, K. Chishiro, et al., J. Am. Chem. Soc. 142 (2020) 7574–7583.
[3] Q.D. Gibson, T.D. Manning, M. Zanella, et al., J. Am. Chem. Soc. 141 (2019) 847–856.
[4] Y. Shi, J. Li, C. Mao, et al., Nat. Commun. 12 (2021) 5923.
[5] F. Chen, Y. Zhang, H. Huang, Chin. Chem. Lett. 34 (2023) 107523.
[6] M. Somekh, A.M. Khenkin, A. Herman, et al., ACS Catal. 9 (2019) 8819–8824.
[7] J. Kang, Y. Zhang, Z. Chai, et al., Adv. Mater. 33 (2021) 2100407.
[8] H. Li, F. Jiang, S. Drdova, et al., Catal. Sci. Technol. 11 (2021) 319–331.
[9] G. Zhan, J. Li, Y. Hu, et al., Environ. Sci.: Nano 7 (2020) 1454–1463.
[10] L. Wang, R. Wang, T. Qiu, et al., Nano Lett. 21 (2021) 10260–10266.
[11] R. Li, Q. Luan, C. Dong, et al., Appl. Catal. B: Environ. 286 (2021) 119832.
[12] L. Wang, X. Zhao, D. Lv, et al., Adv. Mater. 32 (2020) 2004311.
[13] P.A. Hsieh, P.J. Chen, L.M. Lyu, et al., ACS Appl. Mater. Interfaces 13 (2021) 58799–58808.
[14] A. Kuila, P. Saravanan, D. Bahnemann, et al., Appl. Catal. B: Environ. 293 (2021) 120224.
[15] H. Li, F. Qin, Z. Yang, et al., J. Am. Chem. Soc. 139 (2017) 3513–3521.
[16] Y. Li, D. Hui, Y. Sun, et al., Nat. Commun. 12 (2021) 123.
[17] M. Magre, J. Cornella, J. Am. Chem. Soc. 143 (2021) 21497–21502.
[18] S.P. Singh, A. Yamamoto, E. Fudo, et al., ACS Catal. 11 (2021) 13768–13781.
[19] H.W. Moon, J. Cornella, ACS Catal. 12 (2022) 1382–1393.
[20] S. Gong, G. Zhu, R. Wang, et al., Appl. Catal. B: Environ. 297 (2021) 120413.
[21] J. Lu, W. Zhou, X. Zhang, et al., J. Phys. Chem. Lett. 11 (2020) 1038–1044.
[22] H. Wang, W. Zhang, X. Li, et al., Appl. Catal. B: Environ. 225 (2018) 218–227.
[23] W.Y. Huang, Z.Q. Shen, J.Z. Cheng, et al., J. Mater. Chem. A 7 (2019) 24222–24230.
[24] G. Liu, B. Wang, X. Zhu, et al., Small 18 (2022) 2105228.
[25] X. Cao, A. Huang, C. Liang, et al., J. Am. Chem. Soc. 144 (2022) 3386–3397.
[26] S. Jian, Z. Tian, J. Hu, et al., Adv. Powder. Mater. 1 (2022) 100004.
[27] S. Wang, X. Han, Y. Zhang, et al., Small Struct. 2 (2021) 2000061.
[28] W. Fan, C. Li, H. Bai, et al., J. Mater. Chem. A 5 (2017) 4894–4903.
[29] F. Yang, H. Li, K. Pan, et al., Sol. RRL 5 (2020) 2000610.
[30] J. Yoon, J. Kim, F. Tieves, et al., ACS Catal. 10 (2020) 5236–5242.
[31] A. Gopakumar, P. Ren, J. Chen, et al., J. Am. Chem. Soc. 144 (2022) 2603–2613.
[32] L. Zhang, Z. Wang, C. Hu, et al., Appl. Catal. B: Environ. 257 (2019) 117785.
[33] X. Li, B. Kang, F. Dong, et al., Nano Energy 81 (2021) 105671.
[34] X.A. Dong, W. Cui, H. Wang, et al., Sci. Bull. 64 (2019) 669–678.
[35] F. Chen, Z. Ma, L. Ye, et al., Adv. Mater. 32 (2020) 1908350.
[36] L. Liu, J. Liu, K. Sun, et al., Chem. Eng. J. 411 (2021) 128629.
[37] Y. Nalawade, J. Pepper, A. Harvey, et al., ACS Appl. Electron. Mater. 2 (2020) 3233–3241.
[38] J. Li, W. Pan, Q. Liu, et al., J. Am. Chem. Soc. 143 (2021) 6551–6559.
[39] W. Kong, Z. Xing, B. Fang, et al., Appl. Catal. B: Environ. 304 (2022) 120969.
[40] L. Yu, F. Li, J. Zhao, et al., Adv. Powder. Mater. 1 (2022) 100031.
[41] G. Zhou, P. Wang, H. Li, et al., Appl. Catal. B: Environ. 298 (2021) 120525.
[42] H. Li, S. Sun, H. Ji, et al., Appl. Catal. B: Environ. 272 (2020) 118966.
[43] Y. Shi, G. Zhan, H. Li, et al., Adv. Mater. 33 (2021) 2100143.
[44] H. Liu, X. Chang, X. Liu, et al., Environ. Sci. Nano 8 (2021) 2542–2553.
[45] X. Zhang, K. Yue, R. Rao, et al., Appl. Catal. B: Environ. 310 (2022) 121300.
[46] X. Nie, G. Li, S. Li, et al., Appl. Catal. B: Environ. 300 (2022) 120734.
[47] Q. Liu, H. Li, H. Zhang, et al., Chin. Chem. Lett. 33 (2022) 4756–4760.